Soft Matter

PAPER

View Article Online
View Journal | View Issue

Cite this: *Soft Matter*, 2021, **17**, 863

Pressure tunable adhesion of rough elastomers†

Naomi Deneke,‡ Allison L. Chau‡ and Chelsea S. Davis *

Received 1st October 2020,
Accepted 17th November 2020

DOI: 10.1039/d0sm01754j

rsc.li/soft-matter-journal

The ability to control adhesion is critical in various technologies including wearable electronics, pressure sensitive adhesives, and robotic systems. Biomimetic fibrillar structures, random surface roughness, and chemical surface treatments have been employed to modify the adhesion energy of materials used in these applications. However, polymer thin film dewetting has not been investigated as a surface modification tool to control adhesion. In this work, polystyrene thin films are thermally annealed on a polydimethylsiloxane substrate, causing them to dewet and form stiff, microscopic asperities on the soft substrate. The size of the asperities increases with increasing pre-annealing film thickness. Adhesion is quantified by flat-punch normal indentation testing. The largest asperities exhibited a decrease in adhesion to below the sensitivity of the instrument. More interestingly, the surfaces covered with the smallest asperities displayed a pressure-dependent adhesive response. By increasing the normal compressive stress applied prior to separation, the total debonding energy increased monotonically on the smallest asperity-covered surfaces.

1. Introduction

1.1 Adhesion control *via* surface topography

The adhesive response of surfaces can be controlled by altering a material's surface topography; this tuneability is important in applications like soft robotics and pick-and-place microelectronics handling. Various patterning techniques such as microcontact printing, photolithography,[1,2] plasma deposition,[3] and inkjet printing[4] have been used to alter surface properties. While these techniques are common, there are several disadvantages that can hinder industrial scaleup. For example, several complicated processing steps or costly equipment are often required to produce these patterns. One solution that addresses these problems is polymer thin film dewetting which quickly produces small scale roughness over large surface areas with minimal processing.[5,6]

It has long been observed that, for the same material, a rough surface will exhibit a different adhesive response compared to a smooth surface. By changing the topography of a surface, its adhesion strength can be altered.[7] Surface roughness can be random, where asperity size varies over several length scales, or ordered, where patterned surface features have a uniform geometry and size. Random surfaces are often characterized by surface roughness parameters such as center line average,[7] lateral correlation length,[8] root-mean-square,[9] and power spectral density[8,10–12] while ordered surfaces are often characterized by the average dimensions of surface features like wrinkle amplitude or wavelength,[13,14] fibrillar post height or diameter,[15] and asperity spacing.[16] Adhesion can be enhanced or reduced by both random and ordered surface roughness depending on the modulus of the substrate and size of the asperities.[17–20]

Most surfaces are not perfectly flat; they are likely textured with peaks and troughs that make them rough. Surfaces with asperity sizes varying over multiple length scales are defined as randomly rough. While there appears to be total contact at the macroscopic length scale (apparent contact), magnification of the contact line reveals that contact often only occurs at the peaks of each asperity, significantly reducing the actual amount of interfacial contact (true contact). True contact is dependent on the modulus and degree of roughness of the adhered materials. Increasing asperity height or the distribution of asperity heights inhibits full contact as the material surface must deform more to contact the troughs between asperity peaks.[21] Alternatively, decreasing the modulus of a soft solid enhances contact formation as it is easier to deform.[22] While randomly rough surfaces are often associated with decreased adhesion relative to an analogous smooth interface, Fuller and Robert's experiments of smooth rubber spheres of various moduli rolling on roughened Perspex showed that enhanced adhesion can be achieved for low moduli and nano-scale surface roughness due to fast stress relaxation times allowing the rubber to conform to the rough surface and increase interfacial contact area.[18] More recently, surface roughness of biomedical

School of Materials Engineering, Purdue University, West Lafayette, Indiana, 47906, USA. E-mail: chelsea@purdue.edu

† Electronic supplementary information (ESI) available. See DOI: 10.1039/d0sm01754j

‡ These authors contributed equally to this work.

implants have been manipulated to increase soft, biological tissue adhesion to the devices.[23–25]

In contrast to random roughness, surfaces can be fabricated with control of surface features to have ordered roughness. Patterned surfaces have an ordered roughness that can affect adhesion strength. Wrinkles,[13,14,26–28] fibrillar posts,[15,29–31] and pancakes[32] are similar in that they have a discrete, repeating topological pattern. These patterned surfaces have been shown to significantly impact adhesion. For instance, low amplitudes and wavelengths have been shown to enhance adhesion, while high amplitude and wavelength wrinkles have led to a reduction in adhesion.[14] Chan *et al.* posited that this enhanced adhesion was due to increased contact line as opposed to contact area.[13]

Biomimetic structures, specifically fibrillar posts that replicate gecko setae, can greatly enhance adhesion relative to smooth, continuous surfaces of the same material[33] and have even displayed switchable adhesion due to buckling.[34] While these patterned surfaces have been shown to alter the adhesion of soft materials, they are often difficult or expensive to fabricate over large surface areas.[14]

1.2 Thin film dewetting

In the present study, dewetted polymer asperities on an elastomeric substrate are employed to tune adhesion. Polymer thin film dewetting is a phenomenon that arises from surface energy differences between a polymer thin film and substrate. By thermally annealing this bilayer system above the glass transition temperature of the polymer, the film will dewet from the substrate to form droplets with characteristic sizes and spacings. The droplets solidify to form axisymmetric, spherical cap-shaped asperities on the substrate surface upon quenching. Fig. 1(a) displays a schematic of the dewetting process.

The mechanism and physics behind polymer thin film dewetting was first studied by Gunter Reiter, who characterized the resulting patterns.[5,35–38] This complex phenomenon is not only influenced by intermolecular forces but is also affected by the viscoelastic properties of the polymer thin film, the fluid dynamics at the film/substrate interface, and the surface energy of the substrate, all of which affect the resulting dewetting patterns.

Reiter observed a power law relationship between asperity diameter and film thickness.[5] Subsequent works investigated rupture and various dewetting mechanisms as well as dewetting pattern formation.[39,40] The ability to control dewetting patterns utilizing heterogeneous substrates and chemically patterned substrates has also been rigorously studied in the past and has been shown to be an effective strategy.[41–43]

Dewetting of polymer thin films begin through three rupture mechanisms that initiate the dewetting process—spinodal decomposition, heterogeneous nucleation, and homogeneous (thermal) nucleation.[44] Dewetting mechanisms vary depending

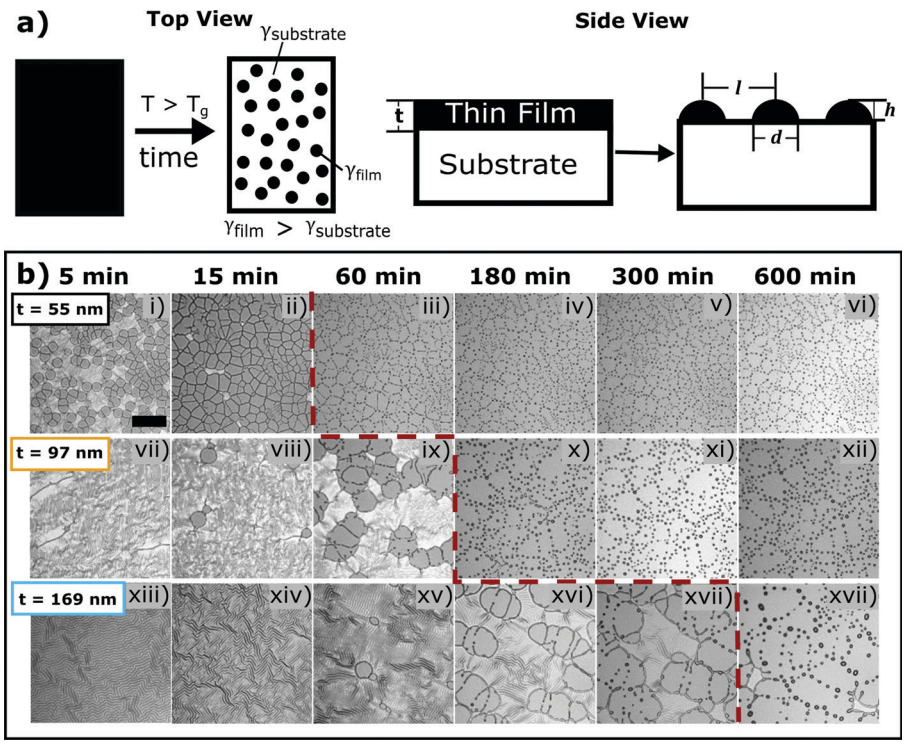

Fig. 1 Dewetted asperity formation on PDMS surfaces. (a) Schematic of the dewetting process. PS asperities are formed by annealing a thin film on a substrate with a dissimilar surface energy over an extended period of time. The side view depicts the control variable, film thickness *t*, and variables that characterize the asperity pattern: asperity spacing, *l*, asperity diameter, *d*, and asperity height, *h*. (b) Optical micrographs of PS thin film dewetting from a PDMS substrate with time. As film thickness increases, *l*, *d*, and *h* also increase. The red dashed line signifies when full dewetting has occurred. Thinner films dewet more quickly than thicker films. The scale bar is 100 μm and applies to all images.

on film thickness. Spinodal dewetting occurs for unstable films, which are usually thinner than 100 nm.[45] In spinodal dewetting, van der Waals forces dominate, and holes are initiated by Laplace and disjoining pressures.[35] This type of nucleation leads to a characteristic polygon pattern of asperities. Homogeneous nucleation, also known as thermal nucleation, requires external energy provided by thermal energy while heterogeneous nucleation relies on external contaminates such as particles, dust asperities or some other defect to act as a nucleation site for dewetting.[44] Film thickness also plays a part in the resulting asperity formation pattern. Once a hole is initiated, it will continue to grow with a dewetting velocity that depends on a variety of factors including polymer viscosity and thermal annealing temperatures.[45,46] As the holes grow, they eventually run into each other to form ribbons of polymer that eventually break up due to Rayleigh–Plateau rim instabilities,[46] forming asperities on the surface. By altering film thickness, polymer viscosity, and surface energy differences between the substrate and polymer, the resulting asperity diameter, height, and areal density vary.

Little research has been performed utilizing polymer thin film dewetting to directly pattern flexible, elastomeric substrates. Past research has focused on utilizing silicon wafers coated with a hydrophobic coating. Han *et al.* concurrently utilized wrinkling and dewetting mechanics to precisely pattern an elastomeric substrate[47] and Song *et al.* utilized poly(dimethyl siloxane) as a substrate and a liquid crystalline polymer as the film.[48]

In the present work, we explore the use of polymer (polystyrene) thin film dewetting on an elastic substrate (poly(dimethyl siloxane)) to create patterned surfaces with the intent of altering the substrate adhesion to develop a pressure tunable adhesive (PTA). We first characterize the surface topography followed by an in depth study of the adhesion of the substrate to a rigid surface observed by flat-punch indentation normal contact adhesion experiments.[49] We show that the size scale of the dewetted asperities on the silicone surface has a dramatic impact on the adhesive response of the interface. More interestingly, we observe a monotonic pressure-dependent adhesive response for the smaller asperities where higher compressive loads prior to debonding result in greater separation forces.

2. Experimental methods and materials

To investigate dewetted thin films for adhesion modification, substrates were prepared by thermally annealing a glassy thin film to initiate dewetting from a silicone elastomer surface. Normal contact adhesion experiments were then performed.

2.1 Dewetted asperity surface preparation

Silicone substrate fabrication. Crosslinked substrates of a thermosetting elastomer, poly(dimethyl siloxane) (PDMS), were used as the substrate. A 5 to 1 by mass mixing ratio of base to curing agent (Dow Sylgard 184) was degassed in a vacuum oven at 25 °C for 10 min. The degassed mixture was poured into a 3 mm deep mold with lateral dimensions of 50 mm by 75 mm and then cured at 120 °C for 5 h. A silicon wafer formed the bottom of the mold to reduce surface roughness. The bulk PDMS was cut into 33 mm by 33 mm squares.

Thin glassy film application to substrate. Glassy polymer thin films of atactic polystyrene (PS) (Polymer Source, Inc., MW = 105.5 kg mol^{-1}, PDI = 1.05) were prepared by spin coating. Film thickness was controlled through the polymer solution concentration (1 wt%, 2 wt%, and 3 wt% PS in toluene, Sigma). Solutions were spin coated onto oxygen plasma-treated silicon wafers (GLOW Research GLOW Plasma System). PS film thickness was measured by interferometry (Filmetrics F20-UV). The films were cut into 25 mm by 25 mm squares. To transfer the PS film, a PDMS square was gently placed on top of the wafer, with care taken to ensure that the cut film section was centered on the PDMS substrate. The wafer and attached PDMS were then submerged in a bath of distilled water and the PDMS substrate was gently separated from the wafer with the PS thin film attached to the PDMS substrate.

Thin film dewetting. PTAs were fabricated by thin film dewetting of the PS thin films from the PDMS substrates. To promote dewetting of the thin films, samples were annealed in a vacuum oven at 165 °C and 762 mm Hg. The samples were removed from the oven at various times throughout this process for imaging and then returned to the oven until the thin film was fully dewetted. A laser scanning confocal microscope (Leica SP8) was utilized for imaging lateral size and spacing of the dewetted asperities. Optical profilometry (Zygo NewView 8300) was used to obtain non-contact measurements of asperity heights (and confirm lateral measurements). The smallest asperities were also characterized with atomic force microscopy (AFM, Veeco Dimension 3100).

2.2 Pressure tunable adhesive surface characterization

As noted previously, substrate topography can significantly impact adhesion. Therefore, analyzing the size, shape, and spatial distribution of dewetted asperities is essential for understanding and predicting adhesion of these rough surfaces. The asperity height, diameter, and spacing were measured to determine the relationship of asperity geometry with film thickness, t.

The final asperity shape varies with t. As film thickness increases, asperity height also increases. PTA fabrication using film thicknesses of t = 55 nm, t = 97 nm, and t = 169 nm yield average asperity heights of $h = 0.5 \pm 0.1$ μm, $h = 1.6 \pm 0.5$ μm, and $h = 2.9 \pm 0.9$ μm respectively; this surface topography is shown in Fig. 2(a). All samples have varying asperity heights that are likely the result of heterogeneous nucleation due to thermally-induced wrinkles (seen in images (i), (vii), and (xiii) of Fig. 1(b)), defects in the film, or contaminants such as dust on the substrate that serve as nucleation sites for dewetting.[44,47] The standard distribution in asperity height increases with increasing film thickness, most likely due to fingering instabilities. Fingering instabilities as seen for the t = 97 nm and t = 169 nm films in images (ix), (xvi), and (xvii) of Fig. 1(b) have been shown to lead to

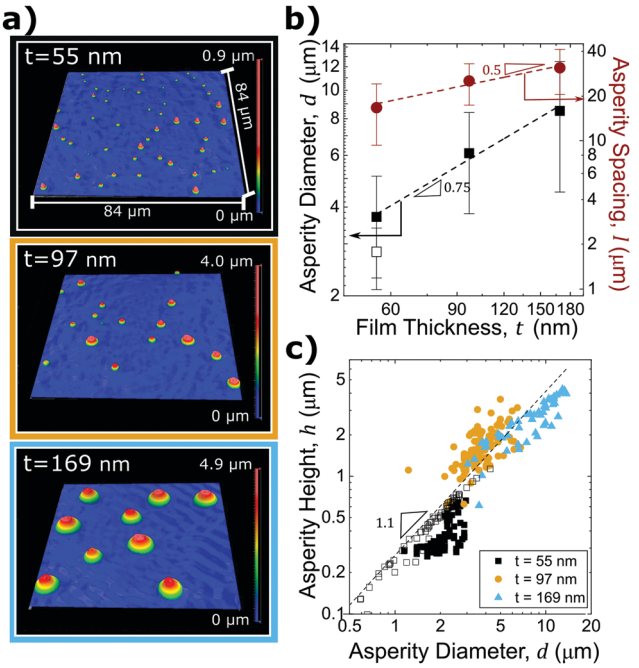

Fig. 2 (a) Optical profilometry images of the dewetted PS asperities. (b) Feret diameter, d and asperity spacing, l, as a function of film thickness, t. The error bars represent one standard deviation. (c) Asperity height, h, as a function of d. Note that the scales in (b) and (c) are logarithmic. Filled symbols represent data collected by optical profilometry and open symbols represent data collected by AFM. The sample size used for each asperity size in plots (b) and (c) is $n \geq 75$.

varying asperity sizes due to irregularities or "flower-like" rim formations during the dewetting process.[50]

The asperity diameter, d, is determined by measuring the longest distance between two points on the PDMS-asperity contact perimeter; this is known as the Feret diameter. Fig. 2(b) displays the relationship between d and t, showing that d also increases with film thickness ($d \sim t^{0.75}$). Additionally, Fig. 2(c) displays h as a function of d and has a power law relationship between asperity height and diameter, $h \sim d^x$, where x is approximately 1.1 (indicating that asperities of various sizes are self-similar). The average asperity aspect ratio (h/d) is 0.24 ± 0.4.

As shown for the individual asperity geometry, the lateral spacing of the asperities also depends on the initial film thickness. Asperity spacing, l, is taken as the center-to-center distance between neighboring asperities in the characteristic polygonal asperity pattern. Smaller satellite asperities are accounted for by determining the distance from each asperity to the two nearest neighbors. Fig. 2(b) shows asperity spacing as a function of film thickness. As film thickness increases, asperity spacing increases as $l \sim t^{0.5}$. Due to the lateral resolution limits of the optical profilometer (OP) used to characterize asperity diameters, atomic force microscopy (AFM) scans were obtained on the smallest asperity PTA surfaces to confirm the average asperity dimensions. While the OP height measurements were in good agreement with the AFM-determined asperity heights, the asperity diameters were dramatically different than those measured with OP. Open symbols plotted in Fig. 2(b and c) signify data collected by AFM. AFM images for t = 55 nm samples are provided in the ESI.†

By altering film thickness and utilizing our understanding of polymer thin film dewetting physics, the resulting asperity geometry can be tuned, facilitating control over the topography of the substrate. This tunable asperity size and spacing can subsequently be utilized to alter the surface properties and geometry of the substrate to create a pressure tunable adhesive.

2.3 Contact adhesion testing apparatus

The contact adhesion tester (CAT) is a custom-built indentation device that vertically translates a probe towards and away from a substrate mounted over an optical microscope. This design allows the simultaneous measurement of the displacement, load, and interfacial contact images over the course of each experiment. The CAT is equipped with a linearly encoded actuator (PI N-381 NEXACT), a load cell with a 100 g capacity (Futek LSB200 S-Beam), and an uncoated aluminosilicate cylindrical flat punch probe (a = 0.5 mm, Edmund Optics) attached in series as shown in Fig. 3(a). The probe approaches the sample surface at a rate of 1 μm s^{-1} to make normal contact, indents the surface until a specified maximum compressive load, P_m, is reached, and finally retracts until full separation of the probe and sample occurs. The device is positioned over an optical microscope (Leica DMi8) to monitor

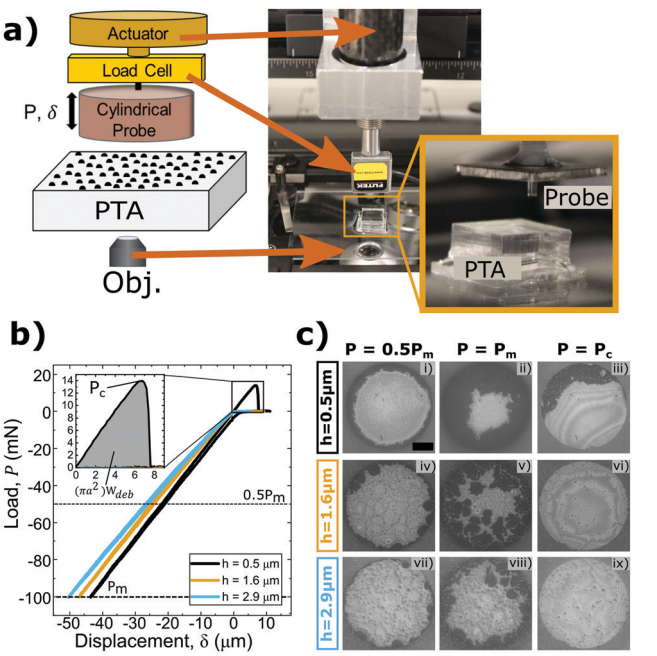

Fig. 3 (a) Schematic of contact adhesion testing device used for indentation testing. (b) Normal contact adhesion testing data for various asperity sizes compressed to P_m = 100 mN. The inset shows the tensile portion of each curve. Only the data for the smallest asperity size is visible as the two larger asperity sizes exhibited no measurable adhesive response. (c) Contact images at various loads for three different asperity sizes. PDMS–probe interfacial contact (darkest regions) decreases as asperity height increases and contact with the PDMS substrate at separation is only observed for the smallest asperity size. The scale bar is 250 μm.

the interfacial contact during testing. Fig. 3(b) displays representative experimental load values as a function of applied displacement for three different asperity sizes. Here, P_m of 100 mN was used for each test. Negative load and displacement values are compressive and positive values are associated with tensile or adhesive loads and vertical positions above the neutral plane of the substrate surface.

3. PTA adhesion results and discussion

3.1 Normal contact adhesion testing

By using a flat punch indenter, or "probe", to perform indentation testing, the energy of debonding between the probe and substrate can readily be determined. In flat punch indentation experiments, a probe is vertically displaced into the substrate until the desired compression of the substrate is achieved and then retracted until separation occurs. Throughout the course of each test, the displacement of the probe is controlled and the normal force acting on the probe is measured. Separation of the probe and substrate occurs when the energy of debonding, U_{deb}, required to separate the two surfaces is equivalent to the stored elastic deformation energy, U_{def}.[49] Therefore, since U_{def} and U_{deb} are equivalent, U_{deb} may be found by integrating the tensile or adhesive portion of the load *versus* displacement curve, $\int P d\delta$ (shaded gray in Fig. 3(b)). An apparent work of debonding, W_{deb}, is found by normalizing U_{deb} by the projected contact area so that

$$W_{deb} = \frac{\int P d\delta}{\pi a^2} \quad (1)$$

where a is the radius of the probe.

3.2 Pressure tunability

Conventional flat punch adhesion tests between two smooth surfaces exhibit full, nearly instantaneous, interfacial contact formation upon approach and rapid, unstable interfacial failure and subsequent separation during retraction. The mechanism by which the probe contacts dewetted PS–PDMS surfaces is quite different. The probe initially contacts the tops of the largest PS asperities on the PDMS surface across the entire projected area of the probe face. Instead of deforming, the glassy polymer asperities are pushed into the more compliant elastomeric substrate as the displacement of the probe continues to indent the surface. Eventually, the asperities are pushed far enough into the PDMS sample for the probe to contact the exposed, dewetted areas of the PDMS surface surrounding the rigid asperities. Contact between the probe and PDMS occurs first around the outer perimeter of the circular probe face, and as the applied compressive load increases further, this interfacial contact area grows radially inward as seen in Fig. 3(c). Boussinesq's solution for the pressure distribution under a flat punch during compression can be used to understand this phenomenon as the pressure is known to be highest at the edge of the contact and lowest at the center for an axisymmetric cylinder indenting an elastic halfspace.[51]

The size of the asperities affects the debonding energy required to separate the probe from the PTA. There is a marked decrease in W_{deb} with increasing asperity size, as shown in Fig. 3(b). For the smallest asperity size (h = 0.5 μm), the sample undergoes tensile deformation due to adhesive forces between the probe and PDMS that keep the interface intact as the probe retracts from the surface. Once a critical pull-off load, P_c, is reached, separation occurs. However, the intermediate (h = 1.6 μm) and largest (h = 2.9 μm) asperity size PTAs do not display similar adhesive responses. Representative contact videos for each of the adhesion tests shown in Fig. 3 are provided in the ESI.† Increasingly larger asperity sizes must be displaced deeper into the PDMS substrate in order to achieve PDMS–probe interfacial contact. Therefore, larger asperities have greater localized stresses at the perimeter of each asperity where localized separation can initiate.

For a more complete analysis of the patterned substrates, multiple adhesion tests were performed on each surface, varying P_m. Fig. 4(a) displays the load *versus* displacement curves for indentation tests on the smallest asperity size sample (h = 0.5 μm) at each compressive load. The areal density, ρ_A, of asperities within the projected contact area is 0.33. The pressure-dependent adhesive response is shown by the increasing tensile responses of the curves where a higher P_m was applied. As P_m increases, P_c also increases, indicating that a greater work of debonding is required to separate the materials. From the images in Fig. 4(b), it is evident that as P_m increases, the maximum PDMS–probe interfacial contact, grows. Hence, pressure tunability is controlled by changes in the amount of interfacial contact that was initially formed. The work of

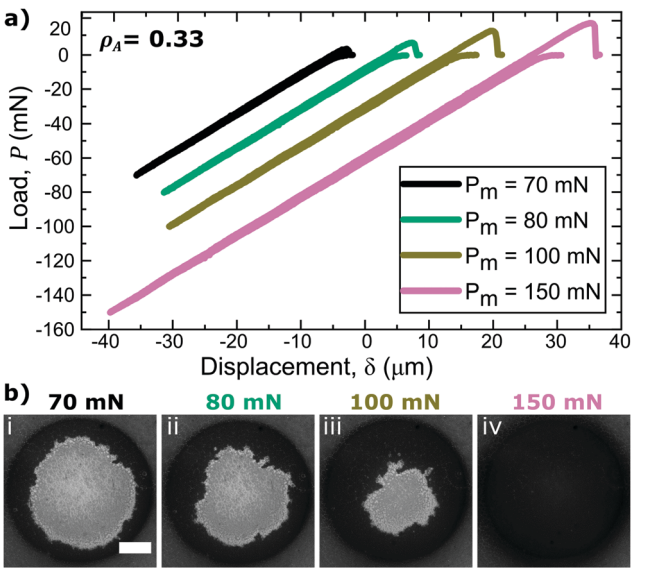

Fig. 4 Load–displacement curves for indentation tests performed on h = 0.5 μm asperity size samples at various P_m (a) and the respective images of PDMS–probe interfacial contact at P_m (b) for surfaces with $\rho_A \approx 0.33$ (similar plots and respective contact images for $\rho_A \approx 0.41$ are presented in the ESI†). Increasing applied loads results in increased interfacial contact apparent full contact is achieved at 150 mN. The scale bar is 250 μm and applies to all images.

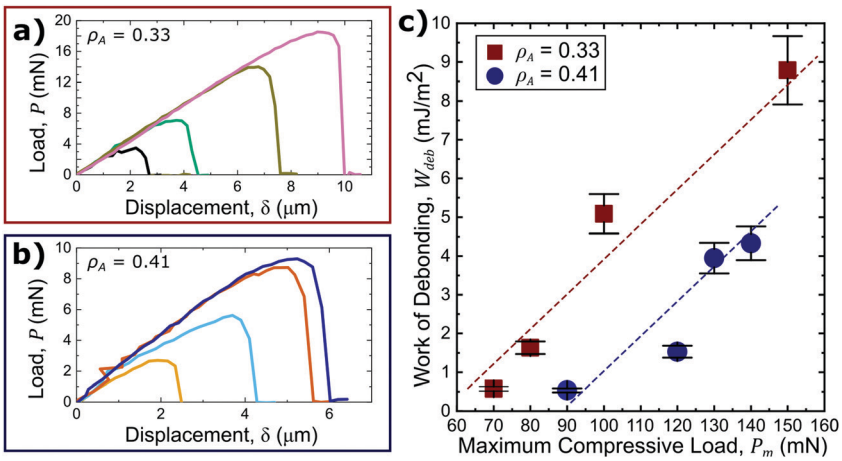

Fig. 5 Insets of the tensile portion of each load–displacement curve plotted for surface with h = 0.5 sized asperities and $\rho_A \approx 0.33$ (a) and $\rho_A \approx 0.41$ (b) outlined in Fig. 4(a) and Fig. S3(a) (ESI†) respectively. Increasingly greater compressive loads result in a greater adhesive response. Integration of each tensile load–displacement curves normalized by the projected contact area to yield W_{deb} (c). W_{deb} is lower for higher ρ_A, but the pressure tuneability remains unchanged. Error bars are 10% error.

debonding for an identical cylindrical probe in contact with smooth, uncoated PDMS is 32 mJ m^{-2} and independent of P_m. The presence of PS asperities on the surface results in a reduction in W_{deb} ranging from 72% to 98% depending on the pre-load.

Interestingly, it was shown that probing a surface with a different areal density of asperities, ρ_A, while holding the asperity size distribution constant, alters the adhesive response. Fig. 5(a and b) present magnified adhesion curves during adhesive deformation of surfaces of the smallest asperity size (h = 0.5 μm) and with a ρ_A of 0.33 and 0.41, respectively. It is evident from the presented data that a larger ρ_A results in a decreased adhesive response (Fig. 5(c)). Upon compression, the dewetted PS asperities are pushed into the PDMS substrate, forming a circumferential depression around each asperity where there is no contact between the probe and any part of the PTA material. The size of the depression is dependent on the size of the asperity and applied load. These depressions are essentially cracks where debonding can initiate. For a region of interest with a higher ρ_A, there will be more of these cracks and more regions of localized stress that can aid in separation. Still, the pressure tunability, taken as the slope of W_{deb} as a function of P_m in Fig. 5(c), is unchanged as ρ_A differs. Therefore, the absolute value of W_{deb} is dependent on the applied load and ρ_A while the pressure tunability is independent of ρ_A for a given asperity size. These results show that multiple adhesive responses can be achieved for a single material by application of rigid, axisymmetric surface asperities, and further control is attainable by changing the areal density of the asperities. From this information, a range of surface topographies can be fabricated with various bilayer material systems to design and obtain a desired PTA response.

4. Conclusion

In this work, the surface of a bulk elastomer, poly(dimethyl siloxane), was patterned by thermally annealing and dewetting a glassy polymer thin film to form rigid, microscopic asperities of polystyrene. Several trends were observed relating the initial film thickness to asperity geometry, enabling control of the size scale of the surface roughness. These dewetted asperities resulted in altered adhesive behavior. A total loss in adhesion strength was observed for the intermediate and largest asperity sizes. However, for the smallest asperity sizes, the separation strength increased with increasing compressive load. This "pressure-tunable" adhesive response is a significant observation in normal contact adhesion science and opens the door for the development of advanced adhesive systems with several levels of adhesive performance attainable with the same surface. For precisely controlled "pick and place" manufacturing applications, the observations presented in this work could form the basis for a new generation of specialty adhesives. Future work will further explore the tuneability of these PTAs and investigate the scaling of P_c with P_m for various surface pattern types. Additionally, the microscopic mechanisms governing the contact formation and separation around individual asperities will be investigated to understand the underlying mechanics that lead to this unique interfacial behavior.

Conflicts of interest

There are no conflicts to declare.

Acknowledgements

We thank E. P. Chan of NIST for interesting discussions that motivated this work. Purdue University provided financial support. ND acknowledges funding support from the George Washington Carver Fellowship (Grant 7100060). AC was supported by the Purdue Office of Undergraduate Research Scholarship.

References

1 D. Tian, Y. Song and L. Jiang, *Chem. Soc. Rev.*, 2013, **42**, 5184–5209.

2 B. Päivänranta, A. Langner, E. Kirk, C. David and Y. Ekinci, *Nanotechnology*, 2011, **22**, 375302.
3 L. Dai, H. J. Griesser and A. W. H. Mau, *J. Phys. Chem. B*, 2002, **101**, 9548–9554.
4 L. Zhang, J. Wu, M. N. Hedhili, X. Yang and P. Wang, *J. Mater. Chem. A*, 2015, **3**, 2844–2852.
5 G. Reiter, *Am. Phys. Soc.*, 1992, **68**, 75–78.
6 Z. Zhang, Z. Wang, R. Xing and Y. Han, *Polymer*, 2003, **44**, 3737–3743.
7 K. N. G. Fuller and D. Tabor, *Proc. R. Soc. A*, 1975, **345**, 327–342.
8 H.-C. Kim and T. P. Russell, *J. Polym. Sci., Part B: Polym. Phys.*, 2001, **39**, 1848–1854.
9 L. Pastewka and M. O. Robbins, *Proc. Natl. Acad. Sci. U. S. A.*, 2014, **111**, 3298–3303.
10 A. Pogačnik and M. Kalin, *Wear*, 2013, **300**, 143–154.
11 V. B. Svetovoy and G. Palasantzas, *Adv. Colloid Interface Sci.*, 2015, **216**, 1–19.
12 B. N. J. Persson, O. Albohr, U. Tartaglino, A. I. Volokitin and E. Tosatti, *J. Phys.: Condens. Matter*, 2005, **17**, R1–R62.
13 E. P. Chan, E. J. Smith, R. C. Hayward and A. J. Crosby, *Adv. Mater.*, 2008, **20**, 711–716.
14 C. S. Davis and A. J. Crosby, *Soft Matter*, 2011, **7**, 5373–5381.
15 L. F. Boesel, C. Greiner, E. Arzt and A. del Campo, *Adv. Mater.*, 2010, **22**, 2125–2137.
16 K. Kargupta and A. Sharma, *Langmuir*, 2002, **18**, 1893–1903.
17 G. A. D. Briggs and B. J. Briscoe, *J. Phys. D: Appl. Phys.*, 1977, **10**, 2453–2466.
18 N. G. Fuller and A. D. Roberts, *J. Phys. D: Appl. Phys.*, 1981, **14**, 221.
19 H. K. Minsky and K. T. Turner, *Appl. Phys. Lett.*, 2015, **106**, 201604.
20 G. Carbone, E. Pierro and S. N. Gorb, *Soft Matter*, 2011, **7**, 5545–5552.
21 B. N. J. Persson and E. Tosatti, *J. Chem. Phys.*, 2001, **115**, 5597–5610.
22 B. N. J. Persson, *Eur. Phys. J. E: Soft Matter Biol. Phys.*, 2002, **8**, 385–401.
23 G. J. Price and P. F. Smith, *Polym. Int.*, 1991, **24**, 159–164.
24 A. Thapa, T. J. Webster and K. M. Haberstroh, *J. Biomed. Mater. Res.*, 2003, **67A**, 1374–1383.
25 A. Thapa, D. C. Miller, T. J. Webster and K. M. Haberstroh, *Biomaterials*, 2003, **24**, 2915–2926.
26 M. Kato, Y. Tsuboi, A. Kikuchi and T.-A. Asoh, *J. Phys. Chem. B*, 2016, **120**, 5042–5046.
27 P.-C. Lin, S. Vajpayee, A. Jagota, C.-Y. Hui and S. Yang, *Soft Matter*, 2008, **4**, 1830.
28 G. Lin, P. Chandrasekaran, C. Lv, Q. Zhang, Y. Tang, L. Han and J. Yin, *ACS Appl. Mater. Interfaces*, 2017, **9**, 26510–26517.
29 R. D. O'Rorke, T. W. J. Steele and H. K. Taylor, *J. Adhes. Sci. Technol.*, 2016, **30**, 362–391.
30 S. Vajpayee, A. Jagota and C.-Y. Hui, *J. Adhes.*, 2010, **86**, 39–61.
31 N. Nadermann, J. Ning, A. Jagota and C.-Y. Hui, *Langmuir*, 2010, **26**, 15464–15471.
32 A. J. Crosby, M. Hageman and A. Duncan, *Langmuir*, 2005, **21**, 11738–11743.
33 N. A. Fleck, S. N. Khaderi, R. M. McMeeking and E. Arzt, *J. Mech. Phys. Solids*, 2017, **101**, 30–43.
34 V. Tinnemann, E. Arzt and R. Hensel, *J. Mech. Phys. Solids*, 2019, **123**, 20–27.
35 G. Reiter, *Langmuir*, 1993, **9**, 1344–1351.
36 G. Reiter, *Macromolecules*, 1994, **27**, 3046–3052.
37 G. Reiter, *Phys. Rev. Lett.*, 2001, **87**, 186101.
38 G. Reiter, M. Hamieh, P. Damman, S. Sclavons, S. Gabriele, T. Vilmin and E. Raphaël, *Nat. Mater.*, 2005, **4**, 754–758.
39 T. G. Stange, D. F. Evans and W. A. Hendrickson, *Langmuir*, 1997, **13**, 4459–4465.
40 K. Jacobs, S. Herminghaus and K. R. Mecke, *Langmuir*, 1998, **14**, 965–969.
41 J. C. Meredith, A. P. Smith, A. Karim and E. J. Amis, *Macromolecules*, 2000, **33**, 9747–9756.
42 L. Xue and Y. Han, *Prog. Polym. Sci.*, 2011, **36**, 269–293.
43 A. M. Telford, S. C. Thickett and C. Neto, *J. Colloid Interface Sci.*, 2017, **507**, 453–469.
44 K. Jacobs, R. Seemann and S. Herminghaus, in *Soft Condensed Matter*, ed. O. K. C. Tsui and T. P. Russell, World Scientific Publishing Co. Pvt. Ltd, 2008, vol. 1, pp. 243–265.
45 T. G. Stange, D. F. Evans and W. A. Hendrickson, *Langmuir*, 1997, **13**, 4459–4465.
46 O. Bäumchen, L. Marquant, R. Blossey, A. Münch, B. Wagner and K. Jacobs, *Phys. Rev. Lett.*, 2014, **113**, 014501.
47 X. Han, J. Hou, J. Xie, J. Yin, Y. Tong, C. Lu and H. Möhwald, *ACS Appl. Mater. Interfaces*, 2016, **8**, 16404–16411.
48 S. E. Song, G. H. Choi, G. R. Yi and P. J. Yoo, *Soft Matter*, 2017, **13**, 7753–7759.
49 K. R. Shull, *Mater. Sci. Eng., R*, 2002, **36**, 1–45.
50 S.-H. Choi Bi-min Zhang Newby and B. Zhang, *J. Chem. Phys.*, 2006, **124**, 054702.
51 J. Boussinesq, *Application des potentiels à l'étude de l'équilibre et du mouvement des solides élastiques*, Gauthier-Villars, France, 1885.